Supplementary Material

Mechanism insight into near-infrared light-driven Cu_2O/WO_2 Ohmic contact photothermal catalysts for high-efficient antibiotic wastewater purification

Jihui Li, Shaodong Sun*, Jieli Lyu, Xiaojing Yu, Jiaqing Zhao, Man Yang, Bian Yang, Qing Yang and Jie Cui*

Engineering Research Center of Conducting Materials and Composite Technology, Ministry of Education; Shaanxi Engineering Research Center of Metal-Based Heterogeneous Materials and Advanced Manufacturing Technology; Shaanxi Province Key Laboratory for Electrical Materials and Infiltration Technology; School of Materials Science and Engineering, Xi'an University of Technology, Xi'an 710048, China

E-mail: sdsun@xaut.edu.cn (S. D. Sun), cuijie@xaut.edu.cn (J. Cui).

Experimental

1 Characterizations

The crystal phase was characterized by a Rigaku D/MAX RAPID II X-ray diffractometer (XRD). X-ray photoelectron spectroscopy (XPS, Thermo Fisher Scientific ESCALAB 250Xi) with a monochromatized Al Kα X-ray source was used to perform the chemical composition. The morphology was characterized by FEI QUANTAFEG-450 field emission scanning electron microscope (SEM). Transmission electron microscopy (TEM), high-resolution transmission electron microscopy (HRTEM), and selected-area electron diffraction (SAED) analysis were performed on JEOL JEM-2100 transmission electron microscopy. Diffuse reflectance spectra (DRS) were tested by an ultraviolet-visible-near-infrared U-4100 spectrophotometer (Hitachi) using $BaSO_4$ as a reference. Photoluminescence (PL) spectra were performed by a FluoroMax-4 fluorescence spectrophotometer (Horiba) with an excitation wavelength of 360 nm. The nitrogen adsorption-desorption curves of the samples were obtained by specific surface and porosity analyzer, and the BET specific surface area can be calculated. The signals of superoxide radical ($\bullet O_2^-$), hydroxyl radical (•OH), hole (h^+) and signet oxygen ($^1O_2$) species were detected by a Bruker EMX nano electron param-magnetic resonance (EPR) spectrometer through using solution of 5, 5-dimethyl-1-pyrrolin-n-oxide (DMPO), 2,2,6,6-tetramethylpiperidine (TEMP) and 2,2,6,6-tetramethylpiperidine-1-oxyl (TEMPO) as spin capturing reagents. As for detecting $\bullet O_2^-$, •OH, h^+ and $^1O_2$ radicals, methanol (MeOH) solution of DMPO, aqueous solution of DMPO, aqueous solution of TEMPO and aqueous solution of TEMP were used respectively. The intermediate products of TC photodegradation were detected by liquid chromatography equipped with mass spectrometry (LC-MS), and the possible photodegradation pathway of TC was deduced. Fotric 628C-L25 (Shanghai Thermal Imaging Technology Co., Ltd) infrared imaging cameras were used to detect temperature change owing to the photothermal effect.

2 Electrochemical measurements

During the electrochemical test, Ag/AgCl was used as the reference electrode, platinum foil was acted as the counter electrode, and the prepared sample was severed as the working electrode. Then, Na_2SO_4 aqueous solution (0.2 M, 150 mL) was applied as the electrolyte solution. To prepare the working electrode, 5 mg samples were first added to 0.5 mL distilled water for ultrasonic dispersion for 10 min, and then 10 μL Nafion was added to the above solution for an ultrasound of 15 min. The above suspension was coated on ITO conductive glass with a surface area of 1 cm × 1 cm. Finally, the sample was dried in air to prepare the as-required working electrode.

3 Photodegradation evaluation

10 mg of sample was added to TC deionized aqueous solution (20 mg/L, 50 mL) and ultrasonic treatment was performed until the sample was uniformly dispersed. Then, the mixture was stirred in dark for 1 h to ensure adsorption-desorption balance. Afterwards, the mixed solution was placed under a 300 W Xe lamplight source ($\lambda >$ 700 nm) at a fixed distance and the light source was turned on to start the photodegradation reaction.

After an interval of 10 min, 4 mL of the mixture was centrifuged at high speed and then the supernatant was aspirated to test the absorbance. The photodegradation rate was calculated by the following formula (see Eq. (1)). Where C_0 represents the initial absorbance after adsorption desorption equilibrium in dark, C represents the real-time absorbance under solar light irradiation.

$$Degradation\ efficiency = \frac{C_0 - C}{C_0} \times 100\% \quad (1)$$

Meanwhile, in order to study the reusability and stability of the catalyst, the WO_2/Cu_2O sample was tested for three recycles with TC solution as pollutant. The cyclic samples can be obtained by continuously collecting and centrifuging the catalysts after three irradiations. Then, the crystal phase and morphology characterization of the recovered WO_2/Cu_2O samples were carried out.

4 Theory calculation

DFT calculations were conducted by the Vienna ab initio Simulation Package (VASP). Generalized gradient approximation of the PBE function was used as the

exchange-correlation function. The cutoff energy was set to 450 eV, and the k-mesh was set to 0.03 2*PI/Angstrom. Structure relaxation was performed until the convergence criteria of energy and force reached 1×10^{-4} eV and 0.03 eV $Å^{-1}$, respectively. During the work function calculations for Cu_2O (111) and WO_2 (011) surfaces, a vacuum layer of 15 Å was constructed to eliminate interactions between periodic structures of surface models.

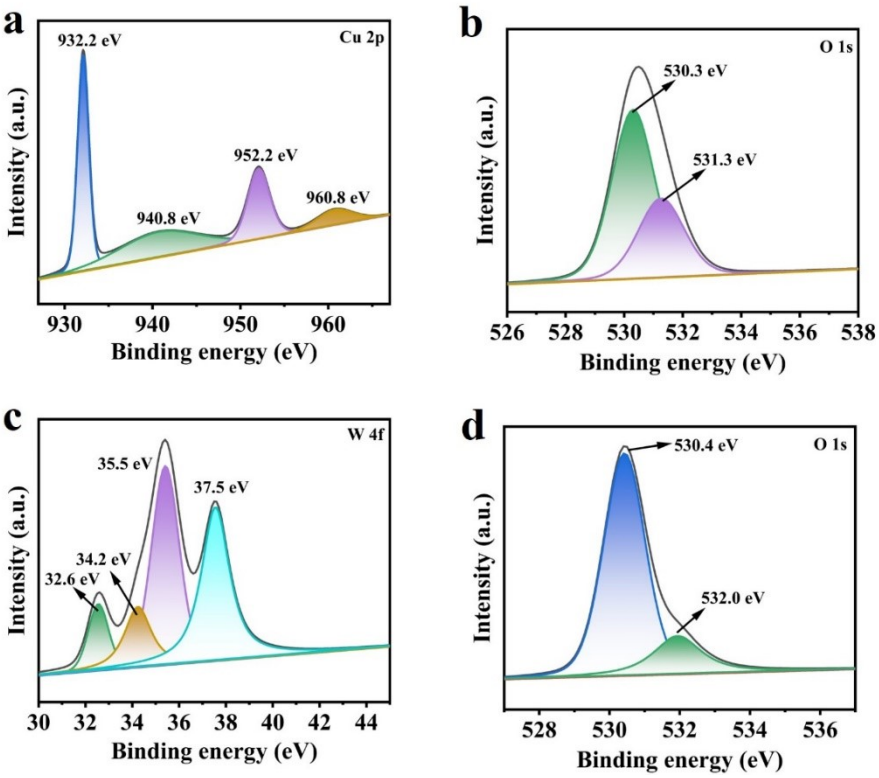

Figure S1. (a) and (b) High-resolution XPS spectra of Cu 2p and O 1s for Cu_2O sample. (c) and (d) High-resolution XPS spectra of W 4f and O 1s for WO_2 sample.

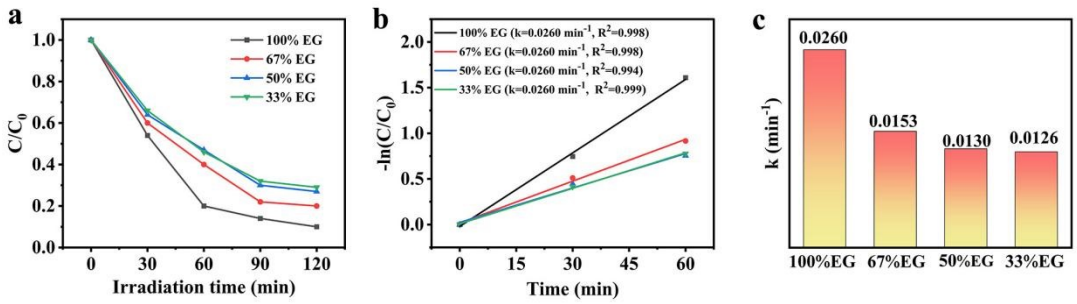

Figure S2. (a) Photodegradation curves under NIR light irradiation, (b) kinetic plots of $-\ln(C/C_0)$ versus time and (c) the corresponding *k* values of the samples synthesized by adding different amount of ethylene glycol.

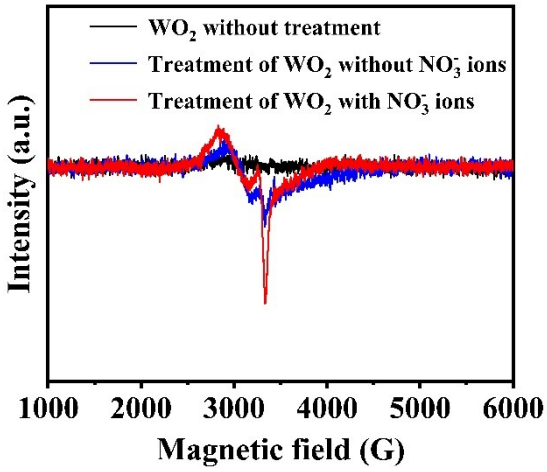

Figure S3. EPR spectra of (a) pristine WO_2 and (b)~(c) WO_2 after treated by EG/glucose/NaOH solution with and without $NaNO_3$ at 90 ^{o}C for 30 min.

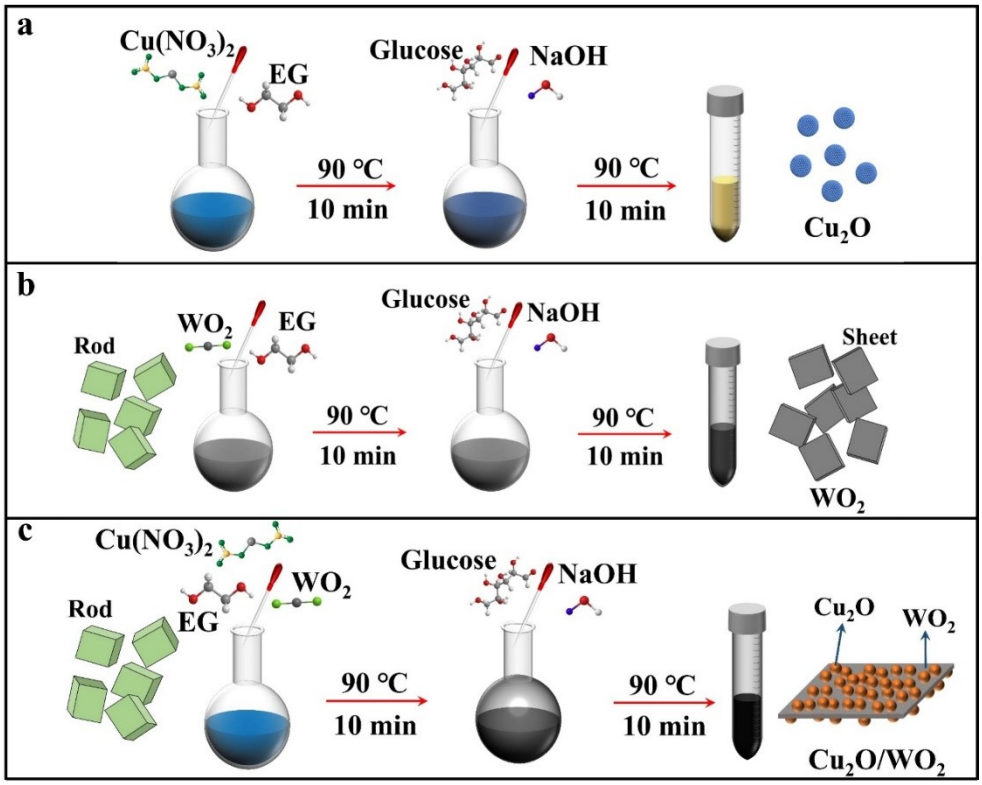

Figure S4. Schematic illustration of the preparation process of different samples. (a) the synthesis of Cu_2O. (b) The treatment of WO_2 samples. (c) The synthesis of Cu_2O/WO_2 composites.

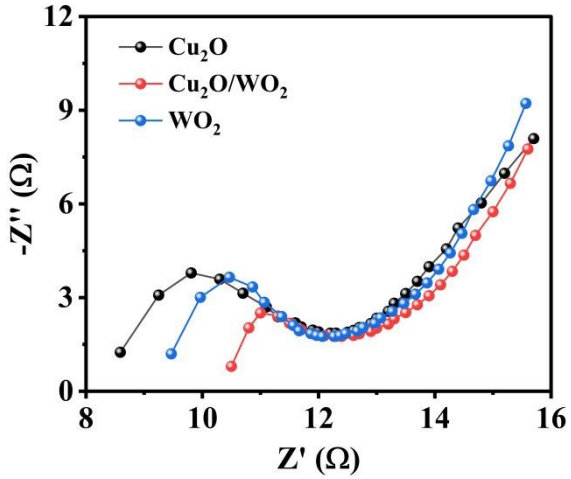

Figure S5. Enlarged high frequency region of EIS spectra of the WO_2, Cu_2O and Cu_2O/WO_2 composites.

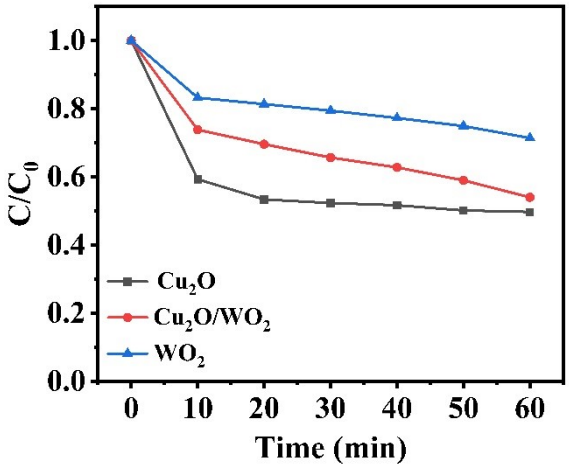

Figure S6. Adsorption curves of the WO_2, Cu_2O and Cu_2O/WO_2 composites in dark.

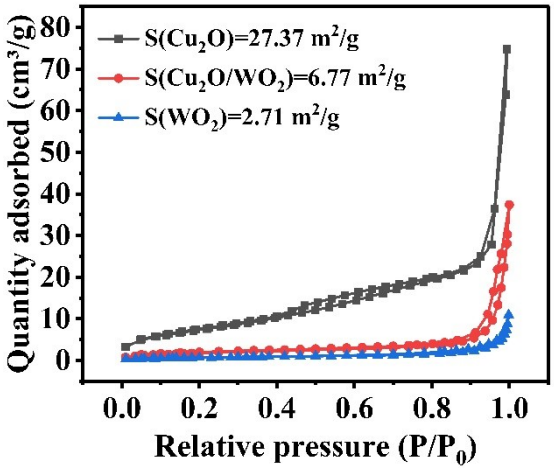

Figure S7. N_2 adsorption-desorption isotherms of the WO_2, Cu_2O and Cu_2O/WO_2 composites, and the inset is the corresponding values of BET surface areas.

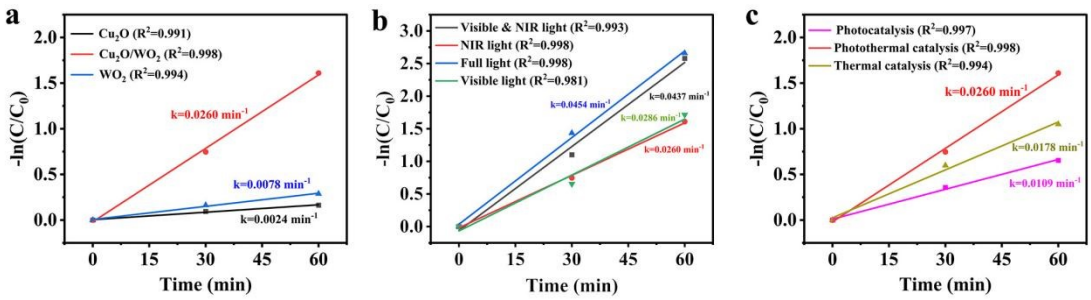

Figure S8. Kinetic plots of -ln(C/C_0) versus time for (a) WO_2, Cu_2O and Cu_2O/WO_2 composites under NIR light irradiation, (b) Cu_2O/WO_2 composites irradiated by NIR, NIR-visible light and full-spectrum solar light, (c) Cu_2O/WO_2 composites under NIR light irradiation at room temperature (photocatalysis), NIR light with natural warming (photothermal catalysis) and keeping heating at 54 ^{o}C without NIR light irradiation (thermal catalysis).

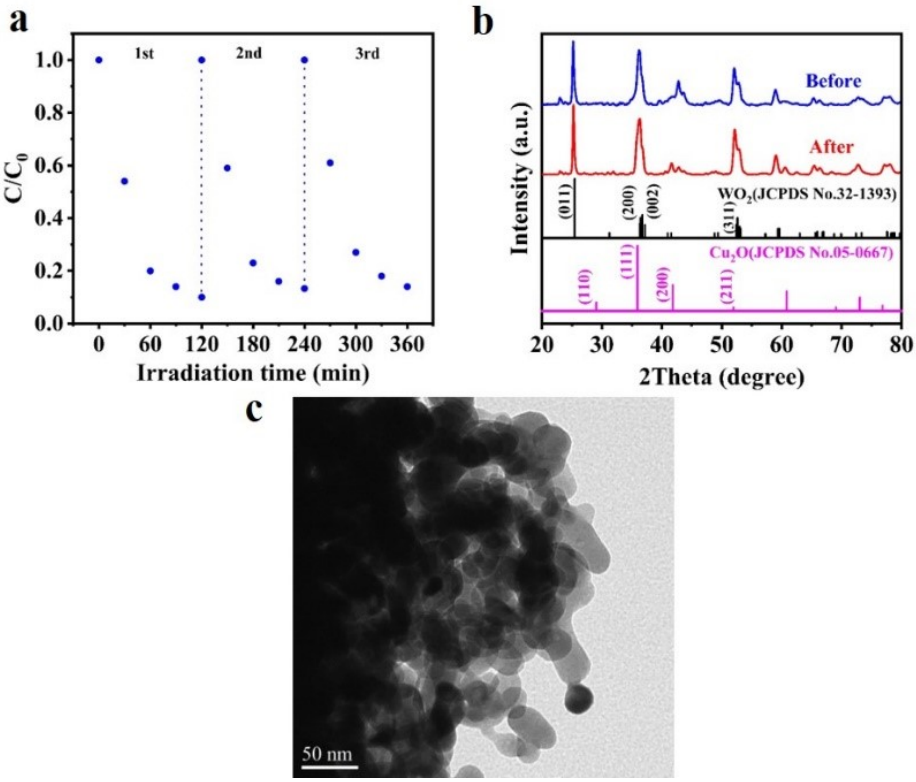

Figure S9. (a) Recycle curves of the as-prepared Cu_2O/WO_2 composites. (b) XRD pattern and (c) TEM image of the as-prepared Cu_2O/WO_2 composites after three cycles.

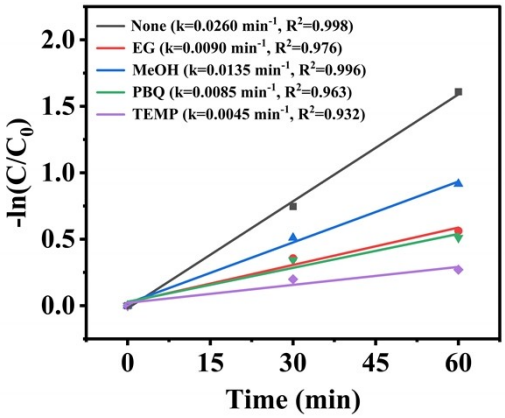

Figure S10. Kinetic plots of -ln(C/C_0) versus time for WO_2, Cu_2O and Cu_2O/WO_2 composites with different radical scavengers under NIR light irradiation.

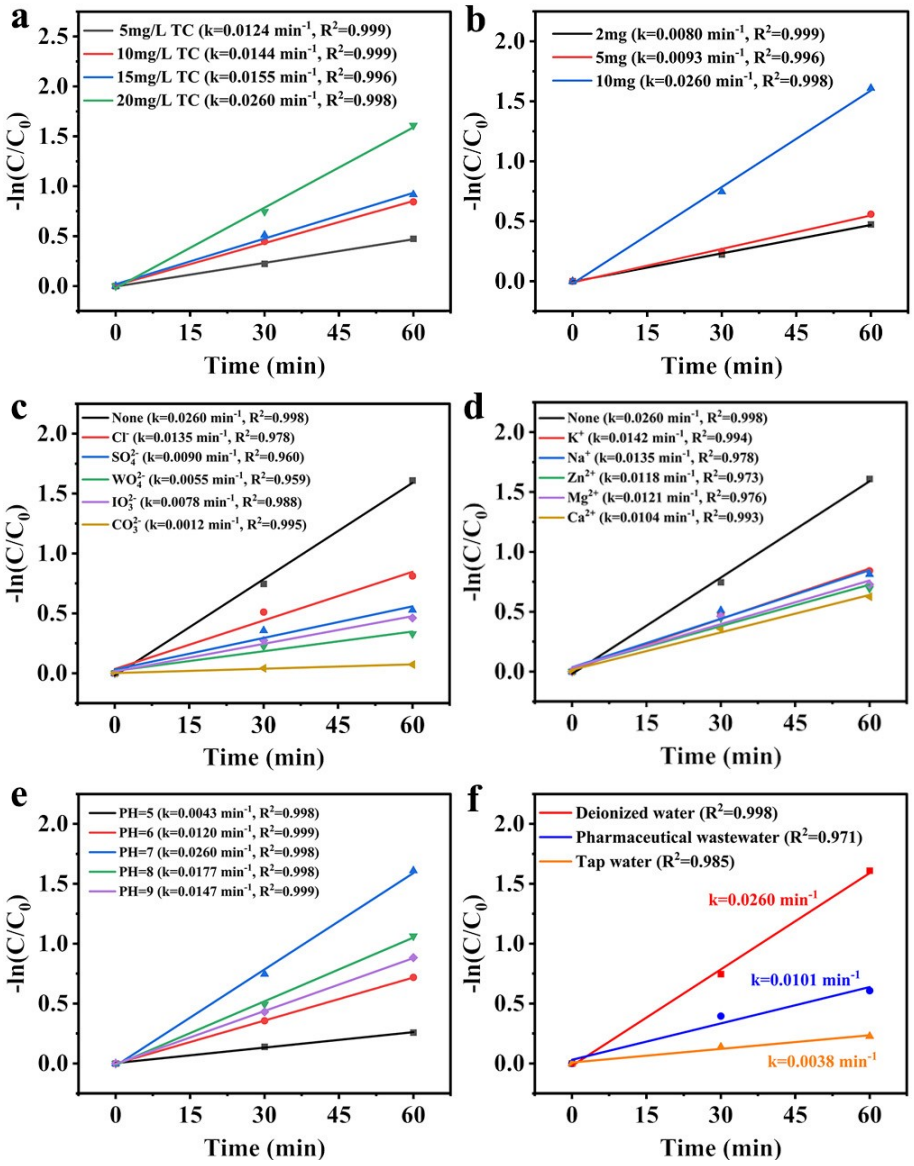

Figure S11. Kinetic plots of -ln(C/C_0) versus time for Cu_2O/WO_2 composites in different (a) TC concentration, (b) mass, (c) anion interfering agents, (d) cation interfering agents, (e) pH values and (f) solvents.

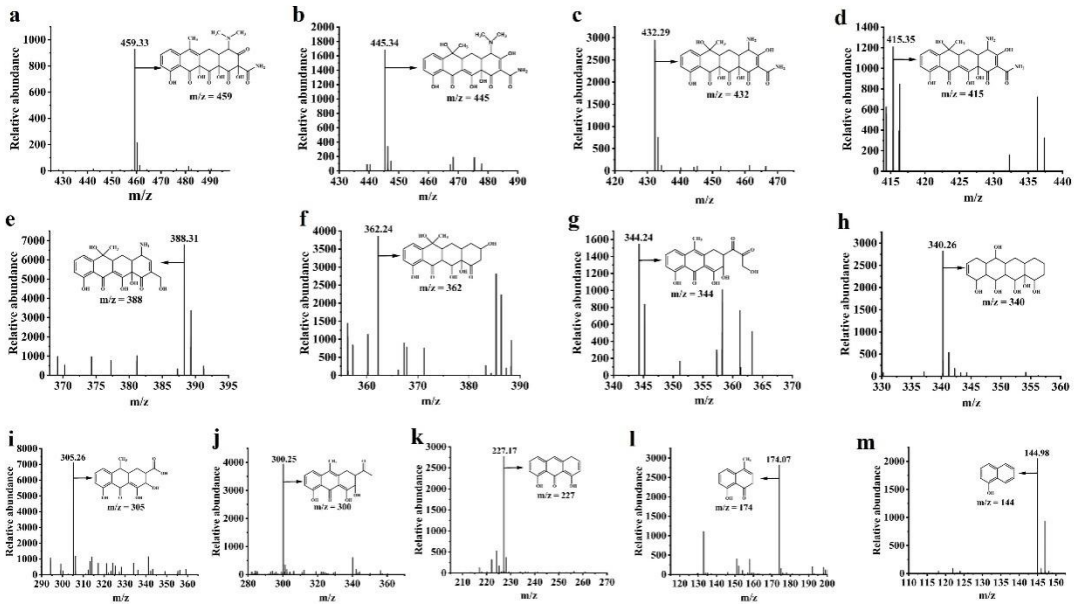

Figure S12. MS spectra of the intermediate products of TC solution.

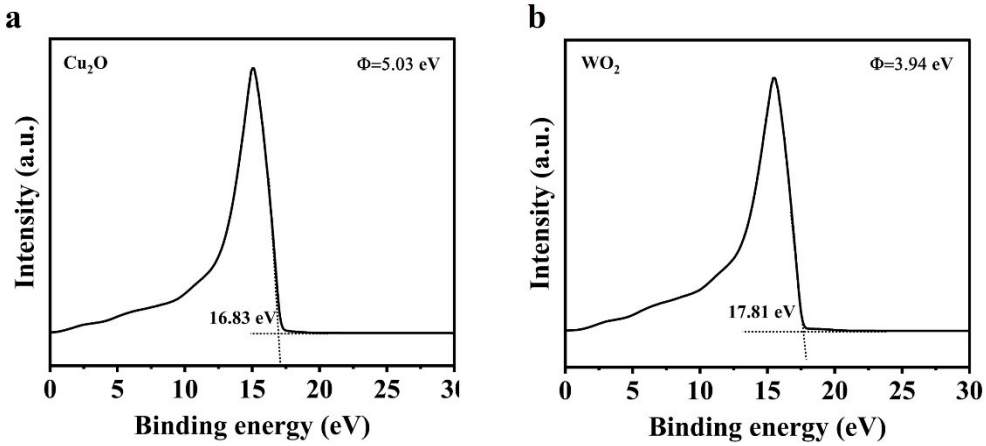

Figure S13. (a) and (b) Ultraviolet photo-electron spectroscopy (UPS) spectra of Cu_2O and WO_2.

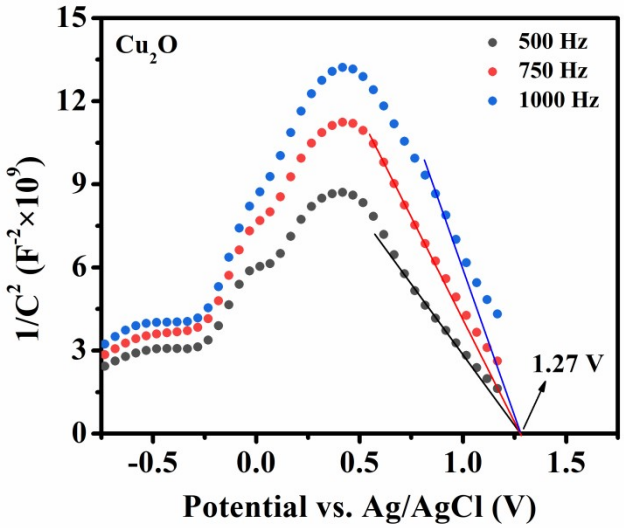

Figure S14. Mott-Schottky plot of Cu_2O.

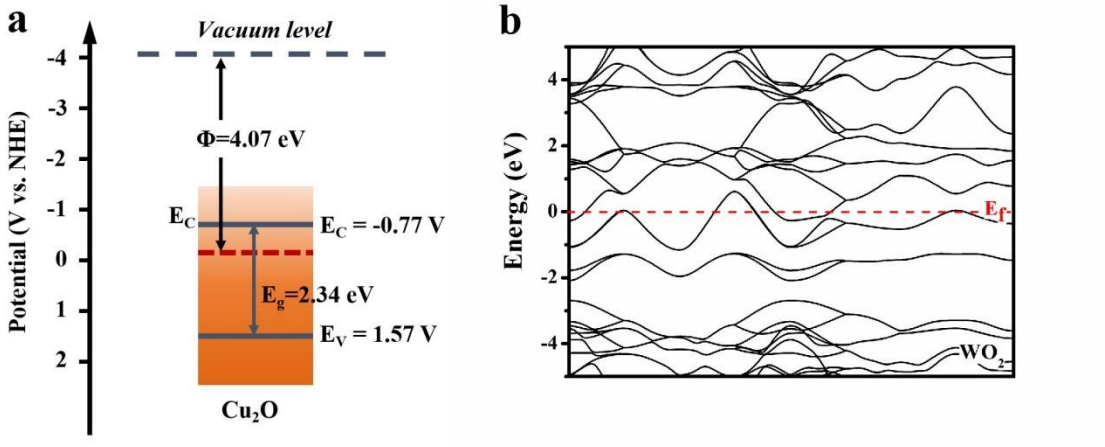

Figure S15. (a) Band potential of Cu_2O, (b) Band structure of WO_2 calculated by DFT, the red dashed line located at zero represents Fermi level.

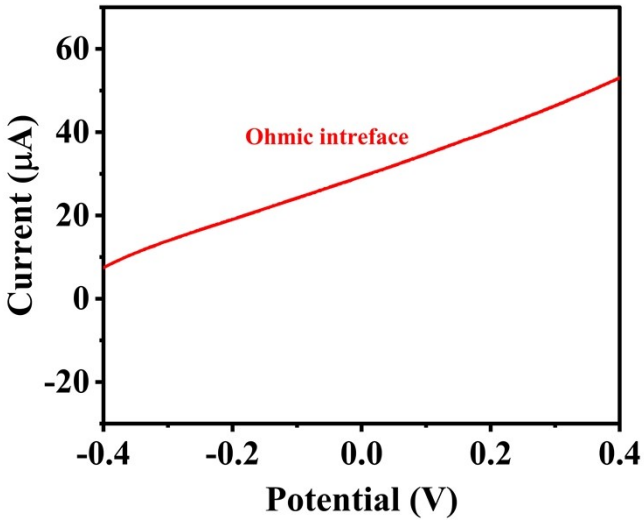

Figure S16. I−V property of Cu_2O/WO_2 Ohmic junction.

Table S1. Comparison of degradation of TC solution with other recently reported catalysts.

Photocatalyst	Wavelength	TC	Volume	Dosage	Time	Efficiency	k (min^{-1})	Reference
WO_2/Cu_2O	**λ>700 nm**	**20 mg/L**	**50mL**	**10 mg**	**120 min**	**91%**	**0.026**	**This work**
(001)TiO_2/Ti_3C_2	λ>780 nm	10 mg/L	50 mL	50 mg	150 min	28.63%	0.00053	**1**
$CuBi_2O_{4-x}/Bi_2O_{2-x}CO_3$	λ>800 nm	20 mg/L	50 mL	50 mg	120 min	43%	0.0065	**2**
CuS/H_2O_2	λ=980 nm	20 mg/L	50 mL	10 mg	80 min	80%	0.0205	**3**
1 wt% Cu-WO_3	λ>800 nm	10 mg/L	100 mL	30 mg	360 min	92.4%	0.00292	**4**
3% CDs/$ZnFe_2O_4$	λ>800 nm	30 mg/L	100 mL	20 mg	120 min	78%	0.0026	**5**
$BiVO_4$/Ag@N-CQDs	λ>760 nm	10 mg/L	100 mL	30 mg	180 min	65.7%	None	**6**
g-C_3N_{4-x}/Bi/$Bi_2O_2(CO_3)_{1-x}(Br,I)_x$	(800 nm < λ< 1500 nm)	20 mg/L	50 mL	50 mg	480 min	70%	None	**7**
Bi_2S_3/C–dots	λ>800 nm	10 mg/L	80 mL	50 mg	60 min	57.9%	None	**8**
BW-$ZnWO_{4-x}$	λ>700 nm	20 mg/L	100 mL	20mg	60 min	83%	None	**9**
5%-CNQDs/Bi_2WO_6	λ>700 nm	20 mg/L,	50 mL	50mg	60 min	40%	None	**10**
BiOBr/CDs/g-C_3N_4	λ>700 nm	20 mg/L	100 mL	20 mg	180 min	17.5%	None	**11**
WO_2/Cu_2O	**λ>420 nm**	**20 mg/L**	**50mL**	**10 mg**	**120 min**	**95.7%**	**0.0454**	**This work**
Bi_2WO_6/C@Cu_2O	λ≥420 nm	10 mg/L	50 mL	20 mg	180 min	88%	0.0035	**12**
CuO@ZnO	λ>420 nm	50 mg/L	50 mL	50 mg	120 min	75.2%	0.0202	**13**
Ag-Cu_2O	λ≥420 nm	20 mg/L	20 mL	5 mg	120 min	90%	0.0198	**14**
CuO-Cu_2O/GO	λ>420 nm	10 mg/L	100 mL	30 mg	120 min	90%	0.0205	**15**
Cu_2O/g-C_3N_4	λ≥420 nm	20 mg/L	100 mL	200 mg	120 min	96.8%	0.0102	**16**
Ti/Fe-Cu_2O	λ≥420 nm	40 mg/L	50 mL	20 mg	60 min	82.5%	0.0306	**17**
Cu_2O/TiO_2	λ≥420 nm	50 mg/L	100 mL	30 mg	60 min	91%	0.0432	**18**
g-C_3N_4/Cu_2O	λ<400 nm	10 mg/L	40 mL	40 mg	40 min	84%	0.0470	**19**
Cu_2O/ZIF-8	λ≥420 nm	50 mg/L	50 mL	20 mg	120 min	84%	None	**20**
MoS_2@Fe_3O_4@Cu_2O	λ≥420 nm	20 mg/L	100 mL	10 mg	80 min	90.3%	None	**21**
Cu_2O/Bi_2WO_6	λ≥420 nm	100 mg/L	10 mL	50mg	180 min	86%	None	**22**
RGO-Cu_2O/Bi_2O_3	λ≥420 nm	10 mg/L	100 mL	50mg	180 min	75%	None	**23**
N-C_3N_4/Cu/Cu_2O	λ≥420 nm	20 mg/L	50 mL	25mg	30 min	84%	None	**24**
g-C_3N_4/Cu_2O	λ>420 nm	30 mg/L	90 mL	100mg	100 min	92.1%	None	**25**
Cu_2O@CuS	λ>420 nm	80 mg/L	100 mL	40mg	120 min	91%	None	**26**

References

[1] Wang Y, Tan G, Feng S, et al. Preparation of exposed (001) facets TiO_2/Ti_3C_2 MXene and

performance of near infrared light photodegradation. Ceramics International, 2023, 49(5): 7258-7265.

[2] Bi Y, Tan G, Zhang B, et al. The enhanced photocatalytic activity of Z-scheme $CuBi_2O_{4-x}/Bi_2O_{2-x}CO_3$ heterojunction towards tetracycline under visible and near-infrared light. Journal of Alloys and Compounds, 2023, 941: 168992.

[3] Huang G Y, Chang W J, Lu T W, et al. Electrospun CuS nanoparticles/chitosan nanofiber composites for visible and near-infrared light-driven catalytic degradation of antibiotic pollutants. Chemical Engineering Journal, 2022, 431: 134059.

[4] Liu X, Wang P, Li Y, et al. Reinforced upconversion and charge separation via mid-gap states in WO_3 nanosheet with infrared light driven tetracycline degradation. Chemical Engineering Journal, 2022, 431: 134134.

[5] Shi W, Gao J, Sun H, et al. Highly efficient visible/near-infrared light photocatalytic degradation of antibiotic wastewater over 3D yolk-shell $ZnFe_2O_4$ supported 0D carbon dots with up-conversion property. Chinese Journal of Chemical Engineering, 2022, 49: 213-223.

[6] Zhang J, Si M, Jiang L, et al. Core-shell Ag@ nitrogen-doped carbon quantum dots modified $BiVO_4$ nanosheets with enhanced photocatalytic performance under Vis-NIR light: Synergism of molecular oxygen activation and surface plasmon resonance. Chemical Engineering Journal, 2021, 410: 128336.

[7] Wang M, Tan G, Ren H, et al. Enhancement mechanism of full-solar-spectrum catalytic activity of $g\text{-}C_3N_{4-x}/Bi/Bi_2O_2(CO_3)_{1-x}(Br, I)_x$ heterojunction: The roles of plasma Bi and oxygen vacancies. Chemical Engineering Journal, 2022, 430: 132740.

[8] Wang Y, Tan G, Feng S, et al. Preparation of exposed (001) facets TiO_2/Ti_3C_2 MXene and performance of near infrared light photodegradation. Ceramics International, 2023, 49(5): 7258-7265.

[9] Osotsi M I, Ling X, Fu S, et al. Bio-inspired $ZnWO_{4-x}$ exhibiting vacancy-driven UV-to-NIR photodegradation of antibiotics in wastewater. Journal of Environmental Chemical Engineering, 2023, 11(2): 109488.

[10] Zhang M, Zhang Y, Tang L, et al. Ultrathin Bi_2WO_6 nanosheets loaded $g\text{-}C_3N_4$ quantum dots: A direct Z-scheme photocatalyst with enhanced photocatalytic activity towards degradation of organic pollutants under wide spectrum light irradiation. Journal of colloid and interface science,

2019, 539: 654-664.

[11] Zhang M, Lai C, Li B, et al. Rational design 2D/2D BiOBr/CDs/g-C_3N_4 Z-scheme heterojunction photocatalyst with carbon dots as solid-state electron mediators for enhanced visible and NIR photocatalytic activity: kinetics, intermediates, and mechanism insight. Journal of Catalysis, 2019, 369: 469-481

[12] Niu J, Song Z, Gao X, et al. Construction of Bi_2WO_6 composites with carbon-coated Cu_2O for effective degradation of tetracycline. Journal of Alloys and Compounds, 2021, 884: 161292

[13] Al-Haddad M, Shawky A, Mkhalid I A. Highly active ZIF-8 derived CuO@ZnO p-n heterojunction nanostructures for fast visible-light-driven photooxidation of antibiotic waste in water. Journal of the Taiwan Institute of Chemical Engineers, 2021, 123: 284-292.

[14] Sun S, Zhang X, Yu X, et al. Unprecedented Ag-Cu_2O composited mesocrystals with efficient charge separation and transfer as well as visible light harvesting for enhanced photocatalytic activity. Nanoscale, 2021, 13: 11867-11877.

[15] Zhang Z, Sun L, Wu Z, et al. Facile hydrothermal synthesis of CuO-Cu_2O/GO nanocomposites for the photocatalytic degradation of organic dye and tetracycline pollutants. New Journal of Chemistry, 2020, 44: 6420-6427.

[16] Sun G, Li X, Xie L, et al. Microwave in-situ liquid-phase deposition of Cu_2O/Tg-C_3N_4 heterojunction for enhancing visible light photocatalytic degradation of tetracycline. Diamond and Related Materials, 2022, 127: 109201.

[17] Ye L, Sun S, Yang X, et al. Mechanism insight into the enhanced photocatalytic purification of antibiotic through encapsulated architectures coupling of crystalline Cu_2O/amorphous TiFe layer double hydroxide. Journal of Materials Science & Technology, 2023, 167: 161-170.

[18] Zhang X, Han D, Dai M, et al. Enhanced photocatalytic degradation of tetracycline by constructing a controllable Cu_2O-TiO_2 heterojunction with specific crystal facets. Catalysis Science & Technology, 2021, 11(18): 6248-6256.

[19] Liu B, Wu Y, Zhang J, et al. Visible-light-driven g-C_3N_4/Cu_2O heterostructures with efficient photocatalytic activities for tetracycline degradation and microbial inactivation. Journal of Photochemistry and Photobiology A: Chemistry, 2019, 378: 1-8.

[20] Zhou Y, Feng S, Duan X, et al. Stable self-assembly Cu_2O/ZIF-8 heterojunction as efficient visible light responsive photocatalyst for tetracycline degradation and mechanism insight. Journal

of Solid State Chemistry, 2022, 305: 122628.

[21] Li W, Zhou G, Zhu X, et al. Magnetic assembly synthesis of high-efficiency recyclable flower-like MoS_2@ Fe_3O_4@ Cu_2O like-Z-scheme heterojunction towards efficient photodegradation of tetracycline. Applied Surface Science, 2021, 555: 149730.

[22] Shen H, Liu G, Zhao Y, et al. Artificial all-solid-state system by RGO bridged Cu_2O and Bi_2WO_6 for Z-scheme H_2 production and tetracycline degradation. Fuel, 2020, 259: 116311.

[23] Shen H, Wang J, Jiang J, et al. All-solid-state Z-scheme system of RGO-Cu_2O/Bi_2O_3 for tetracycline degradation under visible-light irradiation. Chemical Engineering Journal, 2017, 313: 508-517.

[24] Liu Y, Yu H, Cui X, et al. Synthesis of N-C_3N_4/Cu/Cu_2O: New strategy to tackle the problem of Cu_2O photocorrosion with the help of band engineering. Separation and Purification Technology, 2022, 282: 119871.

[25] Zhao Q, Wang J, Li Z, et al. Heterostructured graphitic-carbon-nitride-nanosheets/copper (I) oxide composite as an enhanced visible light photocatalyst for decomposition of tetracycline antibiotics. Separation and Purification Technology, 2020, 250: 117238.

[26] Fu Y, Li Q, Liu J, et al. In-situ chemical vapor deposition to fabricate cuprous oxide/copper sulfide core-shell flowers with boosted and stable wide-spectral region photocatalytic performance. Journal of Colloid and Interface Science, 2020, 570: 143-152.

Table S2. LC-MS data of the intermediate products obtained in degradation of TC by the as-prepared WO_2/Cu_2O composites under NIR light irradiation.

Name	Molecule structure	m/z theory value (g/mol)	m/z real value (g/mol)
TC	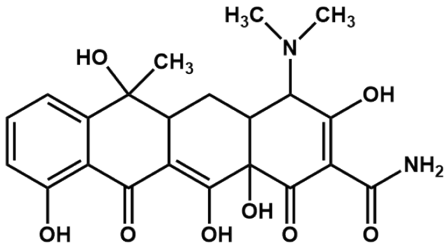	445	445.34
P1	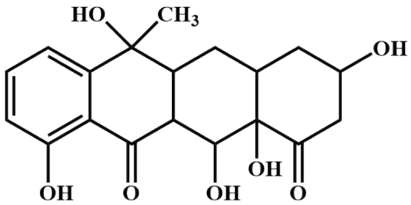	362	362.24
P2	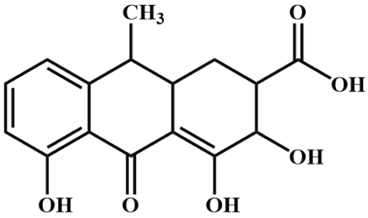	305	305.26
P3	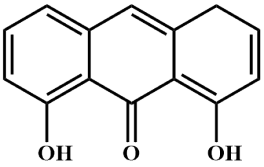	227	227.17
P4	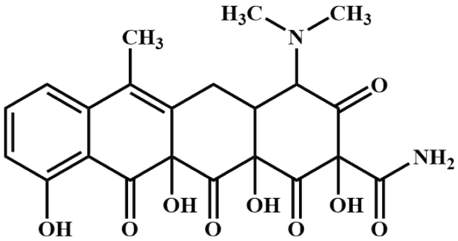	459	459.33
P5	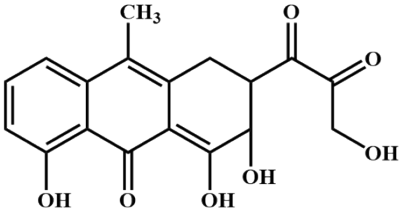	344	344.24

P6	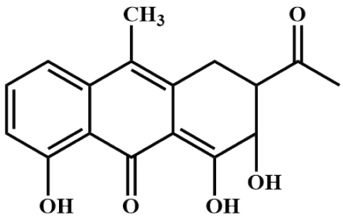	300	300.25
P7	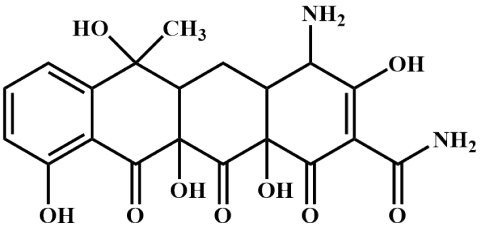	432	432.29
P8	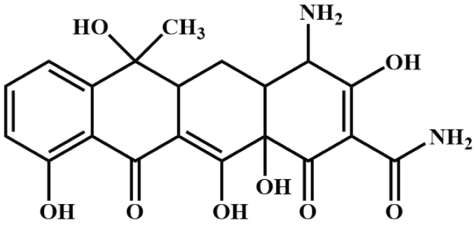	415	415.35
P9	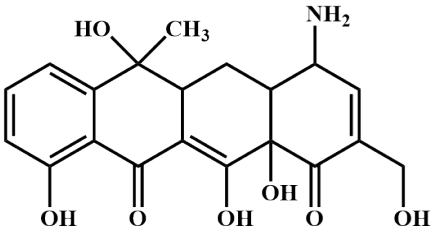	388	388.31
P10	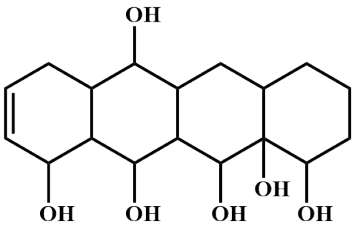	340	340.26
P11	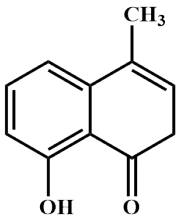	174	174.07
P12	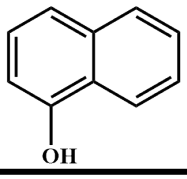	145	144.98